Materials Chemistry and Physics 227 (2019) 368–374

Contents lists available at ScienceDirect

Materials Chemistry and Physics

journal homepage: www.elsevier.com/locate/matchemphys

# Visible-light-driven photocatalytic activities of monodisperse ZnS-coated reduced graphene oxide nanocomposites

Xiaobing Chen[a], He Li[a], Minfang Chen[a], Wenjiang Li[a,*], Zhihao Yuan[a], Rony Snyders[b]

[a] Key Laboratory of Display Materials & Photoelectric Devices, School of Materials Science and Engineering, Tianjin University of Technology, Tianjin, 300384, PR China
[b] Chimie des Interactions Plasma-Surface, University of Mons (UMONS), 20 Place du Parc, 7000, Mons, Belgium

## HIGHLIGHTS

- ZnS nanoparticles were dispersed uniformly on the graphene sheets.
- ZnS-15% RGO exhibited the highest MB degradation rate of 89.43%.
- Visible light photo-activity of ZnS is due to the photosensitization of RGO.

## ARTICLE INFO

*Keywords:*
ZnS
Graphene
Nanocomposites
Photocatalytic activity
Methylene blue

## ABSTRACT

ZnS-Reduced graphene oxide (ZnS-RGO) nanocomposites were successfully synthesized via a facile one-step hydrothermal route, in which ZnS nanoparticles uniformly dispersed on the RGO sheets. The detail structure, morphology and optical properties of as-prepared samples were characterized by X-ray diffraction (XRD), X-ray photoelectron spectroscopy (XPS), field-emission scanning electron microscopy (FESEM), transmission electron microscopy (TEM), Fourier transform infrared (FTIR), Raman spectra, thermogravimetric analysis (TGA), Room-temperature photoluminescence (RT-PL) and UV–vis diffuse reflectance spectra (DRS). The ZnS-RGO nanocomposite containing 15% RGO exhibited the highest visible-light photocatalytic degradation rate for the methylene blue (MB) aqueous solution, and the degradation rate of MB finally reached a maximum of 89.43% after visible-light irradiation for 240 min. However, the pure ZnS with a wide band gap only showed a lower degradation rate of 35.27%. The enhancement of photocatalytic degradation rate is proposal to be due to the photosensitization of graphene illuminated by visible light, in which the photoexcited electrons from graphene can rapidly transfer to the conduction band of ZnS, resulting in improving photocatalytic activity.

## 1. Introduction

Metal sulfide nano-semiconductor composites have received extensive research interest owing to their promising applications in energy storage, gas sensors and photocatalysis [1–3]. Particularly, ZnS with a wide direct band gap is one of typical II–VI group semiconductors, which is considered as an excellent active photocatalyst due to highly negative potentials of excited electrons and strong oxidation [4–7]. For example: Under UV illumination, Singla et al. [8] used highly porous ZnS microspheres deposited with Au and Pt nanoparticles to significantly improve photo oxidation rate of 4-nitrophenol. Xu et al. [9] found that ZnS—CdS nanocomposites could enhance photocatalytic degradation of Rhodamine B aqueous solution. Yin et al. [10] yielded ZnS nanospheres at pH = 7, exhibiting the higher photocatalytic degradation of methyl orange. However, due to the large band gap (3.6 eV), the visible-light photocatalytic efficiency of ZnS is not high enough because of narrow photoabsorption range (ultraviolet light zone), low dispersity and the poor separation efficiency of photoexcited electron-hole pairs [11–13].

Recently, graphene/semiconductor heterogeneous composite photocatalysts were widely constructed for photocatalytic applications [14–16]. It is believed that the coupling of wide-band-gap metal sulfide semiconductor and graphene could create extra visible-light activity, accelerate the charge transfer and enhance the pollutant adsorption [17–20]. Various wide band gap semiconductors have been combined with graphene, exhibiting visible light photocatalytic activity, such as $TiO_2$/RGO [21], ZnO/RGO [22–24] and ZnS/RGO [25–27]. Zhang et al. [28] yielded $TiO_2$-graphene nanocomposites via a hydrothermal reaction, exhibiting much higher photocatalytic activity than the bare $TiO_2$ toward benzene under both UV light and visible light irradiation. Li

* Corresponding author.
*E-mail address:* liwj@tjut.edu.cn (W. Li).

https://doi.org/10.1016/j.matchemphys.2019.01.055
Received 4 September 2018; Received in revised form 17 December 2018; Accepted 23 January 2019
Available online 23 January 2019
0254-0584/ 

et al. [29] prepared graphene-ZnO composites with enhanced photocatalytic degradation of RhB dye under both UV–visible light irradiation. Wang et al. [30] synthesized graphene-ZnS composites, presenting the improved visible light photocatalytic $H_2$-production rate. The mechanism was used to be considered that graphene as a photoexcited electron reservoir of semiconductor, could act as an electron transfer channel to prolong electron-hole pairs lifetime, resulting in improved photocatalytic activity. However, many theoretical calculations and experimental results have demonstrated that the wide band gap of ZnS with the addition of graphene cannot be narrowed to the visible light region. Zhang et al. [31] reported a new role for the visible-light photocatalytic activity of wide band gap ZnS, in which the photosensitization process of graphene was considered to be similar to the organic dye-like photosensitizer. The photoexcited electrons can rapidly transfer from graphene to the conduction band of ZnS.

Herein, ZnS-RGO nanocomposites have been successfully prepared using graphene oxide(GO), $Zn(CH_3COO)_2{\cdot}2H_2O$ and $Na_2S{\cdot}9H_2O$ as raw materials via a facile hydrothermal method, in which ZnS nanoparticles were formed and uniformly dispersed on the surface of reduced graphene oxide (RGO). Meanwhile, the visible-light photocatalytic activity of the obtained composites were further expanded to degrade the methylene blue (MB) in the solution. The effect of graphene content in ZnS-RGO nanocomposites for the degradation of MB aqueous solution was discussed. It can be found that ZnS-RGO nanocomposite containing 15% RGO exhibited the highest degradation rate under visible-light irradiation for 240 min, and the maximum degradation rate of MB could finally reach to 89.43%, On the other hand, the pure ZnS sample presented the lower degradation rate (35.27%) at the same conditions, indicating that the combination of ZnS and RGO enhanced the visible photocatalytic activity of ZnS because RGO might act as a photosensitizer for the wide band gap ZnS semiconductors.

## 2. Materials and methods

### 2.1. Preparation of ZnS and ZnS-RGO nanocomposites

The ZnS-RGO nanocomposites were primarily synthesized by a hydrothermal approach as follows: 0.75 mmol of $Zn(CH_3COO)_2{\cdot}2H_2O$ and different mass content of GO powder (0, 5, 10, 15% of ZnS calculated based on chemical equilibrium reaction) were dissolved into 25 ml deionized water, respectively. Then, the pH value of solution was adjusted to around 9 with ammonia water under ultrasonic treatment. Subsequently, 0.75 mmol of $Na_2S{\cdot}9H_2O$ was dissolved into 15 ml deionized water under ultrasonic treatment. This $Na_2S$ solution was added drop by drop into the mixture solution of $Zn(CH_3COO)_2$ and GO with continuous magnetic stirring for 30 min. Finally, the mixture solution was transferred to a 50 ml Teflon-lined autoclave at 180 °C for 12 h. The reaction products were washed with deionized water and absolute ethanol for several times, and then treated by vacuum freeze-drying to obtain the ZnS-RGO nanocomposites with different weight RGO, named, pure ZnS, and RGO-(5, 10, 15%) ZnS, respectively. The schematic illustration for the synthesis of ZnS-RGO nanocomposites is shown in Scheme 1.

### 2.2. Optical property

Diffuse reflectance spectra is generally analyzed via the Kubelka-Munk function. The band gap energy values of the samples were calculated by the following formula based on the Kubelka Munk function transformation:

$$(Ahv)^2 = B(hv - E_g) \quad (1)$$

where $h$ is the Planck constant, $v$ is the frequency of light, $B$ is a material-related physical quantity, $E_g$ is the band gap energy, $A$ is the absorbance.

For each photocatalytic reaction, 20 mg of photocatalysts (pure ZnS, ZnS-5%RGO, ZnS-10%RGO and ZnS-15%RGO) were respectively added into 50 mL MB aqueous solution (20 mg/L). Before visible-light photocatalytical experiments, MB aqueous solution (20 mg/L) with samples were stirred in the dark for 30 min, to establish the adsorption - desorption equilibrium of the MB on the photocatalysts without visible light irradiation (adsorption region: − 30-0min). Since visible-light photocatalytical reactions were not conducted within first 30 min, single adsorption region time were named as minus 30 - 0 min. Then, the mixture solution was irradiated for different time intervals (photocatalytic region: 0–240 min) under visible light irradiation (300 W xenon lamp source with light filter simulating full spectrum of sunlight). After specific time intervals, 3 ml suspensions were extracted and centrifuged. The UV–Vis spectrophotometer was used to calculate the concentration of MB solution by measuring the absorbance of supernatants. The degradation rate of MB was calculated by the following formula:

$$\text{Degradation}\ (\%) = (1 - A_t/A_0) \times 100\% \quad (2)$$

where $A_0$ and $A_t$ represent the initial absorbance and the absorbance after $t$ minutes, respectively.

### 2.3. Characterization

The crystal phase of the ZnS-RGO composites were characterized by X-ray diffractometer (D/Max2500pc) using a Cu Kα radiation ($\lambda = 0.154056$ nm) at a scan rate of 0.02° 2θ $s^{-1}$. The accelerating voltage and the applied current were 40 kV and 150 mA, respectively. The composition and valence state of the elements for the samples were studied by X-ray photoelectron spectra (XPS) measurements (K-Aepna). The surface morphology and particle size of the samples were investigated by field emission scanning electron microscopy (FESEM) and transmission electron microscopy (TEM). The thermal stability and product purity were studied by thermogravimetric analysis (TGA). Fourier transform infrared spectra (FTIR) were recorded on a Perkin-Elmer spectrometer using KBr pellets. Raman spectra were recorded on a Raman spectrometer using an excitation laser of 532 nm wavelength. Room-temperature photoluminescence (RT-PL) measurements were performed on the solid particles with a pulsed Xe laser (RF-5301 PC) as the excitation wavelength of 330 nm. UV–vis diffuse reflectance spectra (DRS) of the samples were recorded by a UV–vis spectrophotometer (TU-1980) over a wavelength range of 250–800 nm using $BaSO_4$ as the internal reflectance standard.

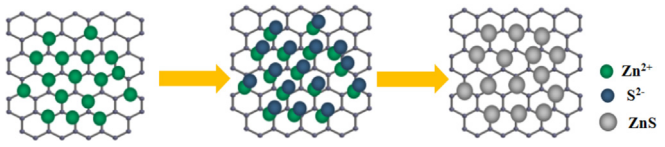


**Scheme 1.** The schematic illustration of the synthesis of ZnS-RGO.

## 3. Results and discussion

X-ray diffraction (XRD) patterns of GO, RGO and ZnS-RGO samples are exhibited in Fig. 1. It is observed from Fig. 1a that a sharp peak arose around 9.05° in the pattern of GO, which is the characteristic peak of GO. After the hydrothermal process, the diffraction peak of GO at 9.05° disappeared and a broad peak at 25° of RGO appeared in the XRD pattern, indicating that GO was reduced to RGO because of the less oxygen-containing functional groups [31]. For the ZnS-RGO samples with different weight ratios of RGO, the XRD patterns are similar to that of pure ZnS. There are five relatively strong peaks at 27.08°, 28.56°, 30.62°, 47.64° and 56.50° from Fig. 1b, which is indexed to (100), (002), (101), (110) and (112) crystal planes of the wurtzite-phase ZnS (JCPDS NO.36–1450) [32]. Meanwhile, no characteristic peaks of RGO can be seen in the patterns of ZnS-RGO samples, which might be

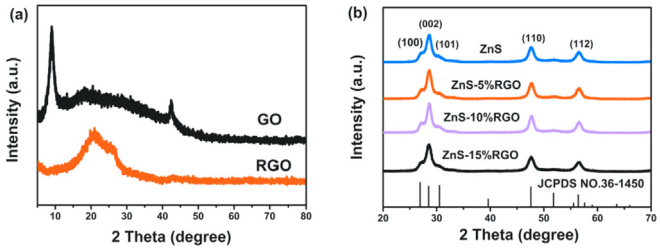


**Fig. 1.** (a) XRD patterns of the pristine GO and RGO, (b) XRD patterns of pure ZnS and ZnS-RGO with different weight ratios of RGO.

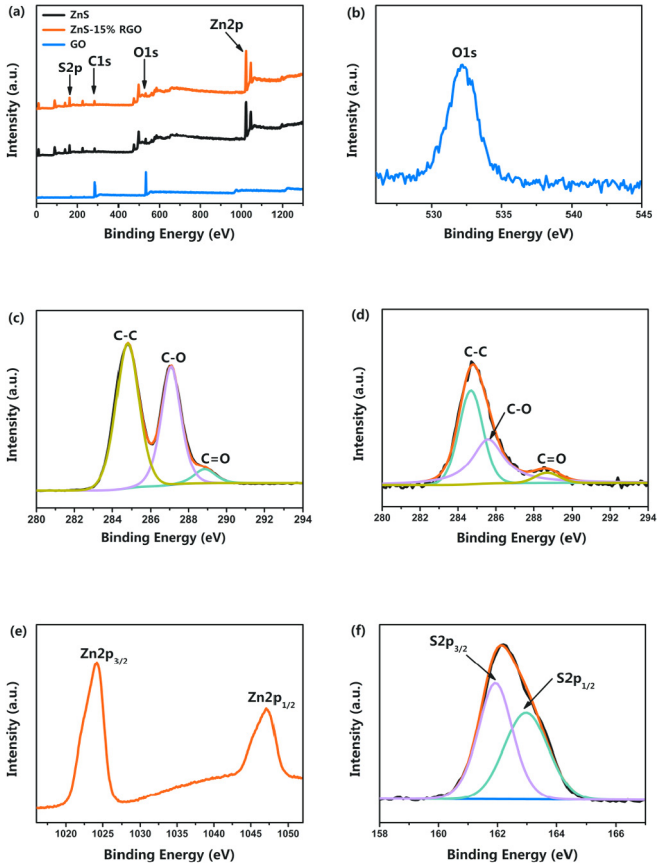


**Fig. 2.** XPS spectra of the different samples: (a) XPS full spectra; XPS spectra of ZnS–15%RGO: (b) O1s, (d) C1s, (e) Zn2p, (f) S2p; XPS spectra of the pristine GO: (c) C1s.

ascribed to the low graphene content in the ZnS-RGO composites. The XRD patterns of ZnS-RGO samples further demonstrate that the growth of ZnS crystal orientations is not affected by RGO, which only provides a growth platform for ZnS [31,32].

X-ray photoelectron spectroscopy (XPS) analysis is used to study the elemental composition and chemical state of the samples (Fig. 2). XPS survey spectrum of the ZnS-15%RGO sample reveals the presence of C, Zn, S and O elements (Fig. 2a). The binding energy at 532.1 eV was assigned to the characteristic peaks of O1s (Fig. 2b). High resolution XPS spectrum of C1s for GO and ZnS-15%RGO samples are shown respectively in Fig. 2c and d. Three strong peaks at 284.8 eV, 287.0 eV and 288.8 eV were corresponding to the C—C, C—O and C=O [33], respectively. The peak intensities of the C—O and C=O in the ZnS-15% RGO spectrum were clearly weaker than that in the pristine GO spectrum, which confirms that GO was sufficiently reduced to RGO after hydrothermal reaction [31–34]. Fig. 2e and f show high resolution XPS peak of Zn 2p and S 2p for the ZnS-15%RGO sample, respectively. The binding energies at 1024.1 eV and 1047.1 eV were assigned to the characteristic peaks of $Zn2p_{3/2}$ and $Zn2p_{1/2}$, respectively, proving that the Zn ions were in the +2 oxidation state. The binding energies at 161.9 eV and 162.9 eV could be assigned to S $2p_{3/2}$ and $2p_{1/2}$, respectively, meaning that the existence of Zn—S bonds in the composites [34].

Fig. 3 shows FESEM images of GO, ZnS, and ZnS-15%RGO samples. The morphology of pristine GO is like many blooming flowers one after another with a curly and ripple structure (Fig. 3a). Compared with ZnS-RGO samples, the pure ZnS nanoparticles synthesized (Fig. 3b) shows an agglomeration tendency to form larger ZnS nanoparticles. It can be observed from Fig. 3c and d, ZnS nanoparticles were spread homogeneously and closely on the surface of graphene in the ZnS-15%RGO sample [33]. As is shown in Fig. 4a and b, ZnS nanoparticles could grow very well on the RGO nanosheets. The average diameter of ZnS particles (measured 100 particles) was about 9.27 nm obtained from TEM statistics (Fig. 4d). The interplanar spacing of 0.31 nm, measured from lattice fringes by high resolution TEM, could be corresponding to the (002) orientation of wurtzite ZnS (Fig. 4c) [35]. The combination of SEM and TEM confirms that the ZnS nanoparticles have a good interfacial contact with RGO sheets, which should be good for the charge carrier transfer [36].

The FTIR spectra of GO and ZnS-RGO samples are shown in Fig. 5. The characteristic peaks of pristine GO: the O—H, C=O, C=C, C—OH and C—O stretching vibrations at 3403, 1725, 1628, 1193 and 1046 $cm^{-1}$, respectively; the O—H bending vibrations of C—OH at 1382 $cm^{-1}$ and the absorption peaks of epoxide group at 584 $cm^{-1}$ [34,37]. Almost all the absorption peaks of oxygen-containing functional groups weakened or vanished obviously for ZnS-RGO samples, which means GO was reduced to RGO after the hydrothermal reaction, consistently with XPS analysis. The Raman spectra of GO and ZnS-15% RGO are shown in Fig. 6. The G band is a measure of C—C bonds of $sp^2$-hybridized GR, and the D band is dominated by various kinds of local defects [35,36]. D band and G band of pristine GO were located at 1353.41 $cm^{-1}$ and 1593.18 $cm^{-1}$, respectively. Owing to the reduction of GO, D and G bands moved to low wavenumbers, which were centered at 1342.87 $cm^{-1}$ and 1584.18 $cm^{-1}$, respectively. In addition, the $I_D/I_G$ (the intensity of D band compared to G band) ratios of the pure GO and the ZnS-15%RGO are 0.90 and 1.09, respectively. An increase of the $I_D/I_G$ ratio means a rise of various types of defects and $sp^2$-hybridized bonds after the hydrothermal reaction. It is in accordance with reported by Pan et al. [34] and Sookhakian et al. [37]. The FTIR and Raman spectra further proves that GO of the ZnS-RGO samples is efficiently reduced to RGO after the hydrothermal reaction.

Fig. 7 shows the TGA curves of the samples to quantify the reduction degree of GO. According to the plot, the weight loss of pristine GO was close to 100 wt% when the temperature was up to 610 °C. There should be three reasons: the evaporation of chemically adsorbed small water molecules from room temperature to near 100 °C, the loss of oxygen-containing functional groups from 100 to 300 °C and the degradation of the carbon-chain framework from 300 to 610 °C [32]. The mass loss is very low for ZnS sample, which is ascribed to the oxidation of ZnS to the ZnO. With regard to ZnS-15%RGO sample, a characteristic weight loss from 100 to 300 °C was a small percent of only 5%, which is attributed to the degradation of the remaining oxygen-containing functional groups, revealing that GO was sufficiently reduced to RGO [38].

The PL spectra of different samples with the excitation wavelength of 330 nm is shown in Fig. 8. Pure ZnS exhibited a stronger PL intensity compared with ZnS-RGO samples. It is attributed to the higher recombination rate of photo-induced electron-hole of pure ZnS. Moreover, ZnS-15%RGO exhibited a lower PL intensity, which indicates photo-induced electron-hole pairs of ZnS-RGO composites were efficiently separated. It is beneficial to enhance the photocatalytic performance [37].

The UV–vis diffuse reflectance spectra (DRS) of the samples are shown in Fig. 9a. It can be found that the amount of RGO in ZnS-RGO samples affects the light absorption for ZnS-RGO samples. With the

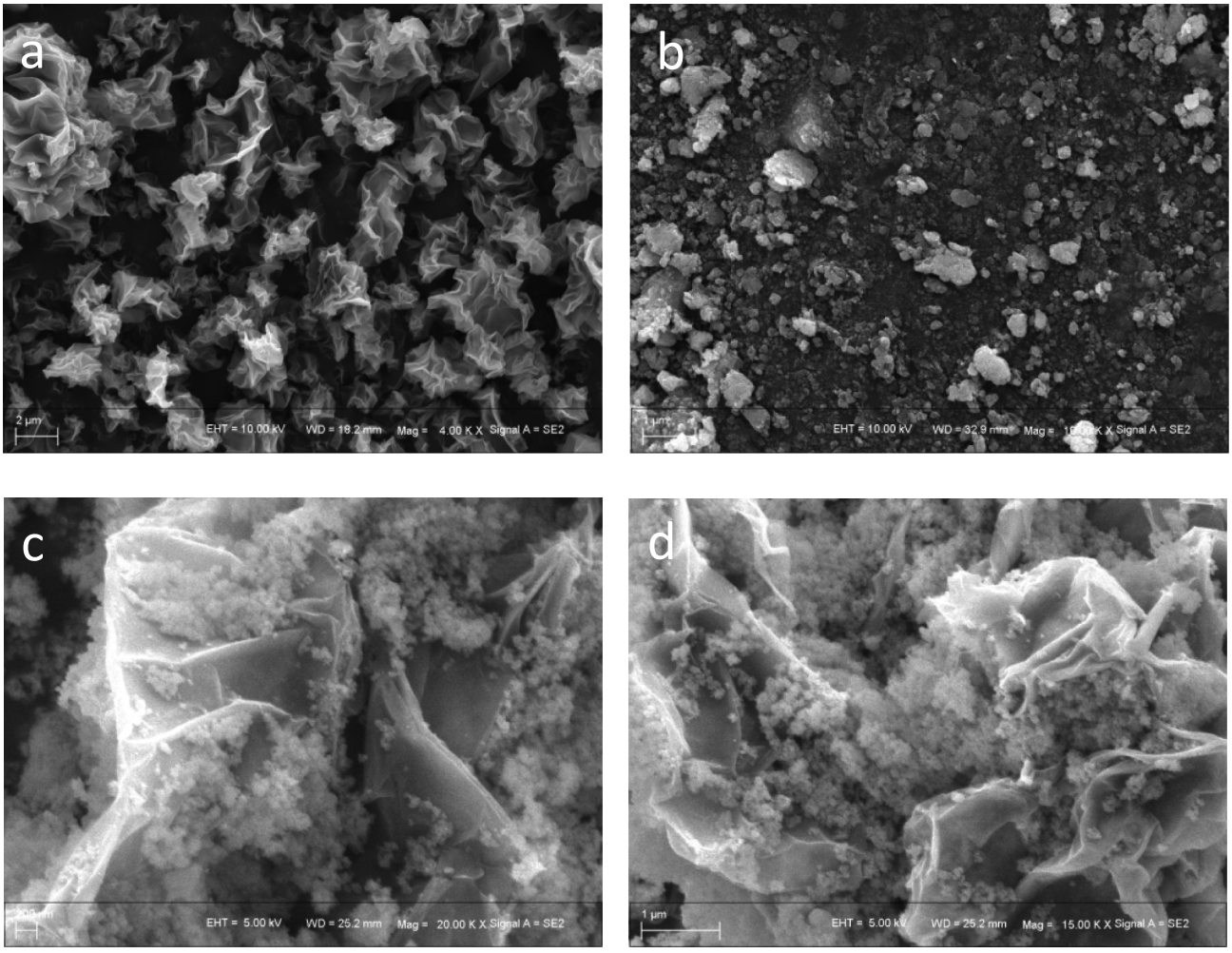


**Fig. 3.** FESEM images of (a) pristine GO, (b) pure ZnS and (c,d) ZnS-15%RGO.

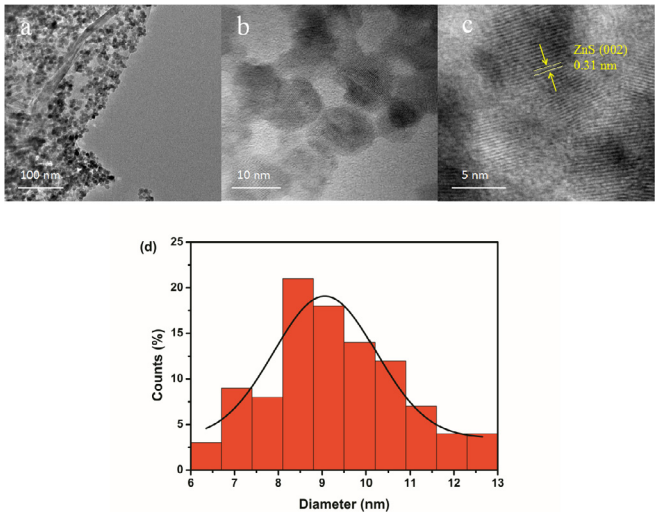


**Fig. 4.** TEM images of ZnS-15%RGO: (a) low-resolution TEM image, (b,c) high-resolution TEM image, (d) the particle size distribution obtained from TEM statistics.

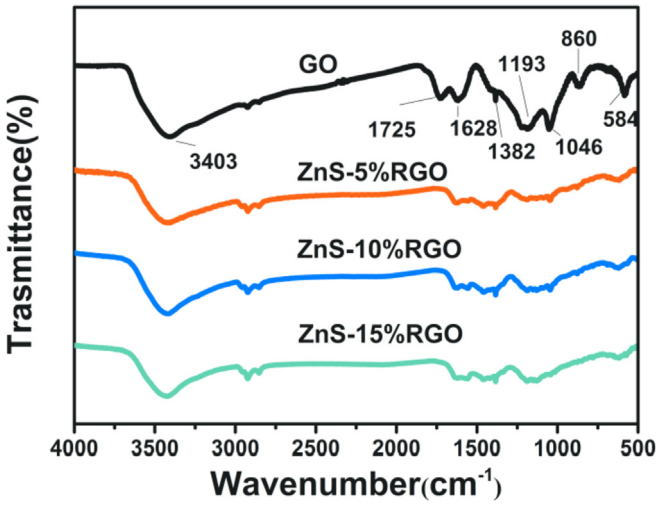


**Fig. 5.** FTIR spectra of the pristine GO and ZnS-RGO with different weight ratios of RGO.

weight ratio of RGO increasing, it is observed the light absorbance of ZnS-RGO samples were increased in the visible light region (from 400 nm to 800 nm). Fig. 9b shows the band gap analysis plot obtained via the transformation based on the Kubelka Munk function. The estimated band gap values of the samples are 3.43, 3.40, 3.33, and 3.25eV respectively for pure ZnS, ZnS-5%RGO, ZnS-10%RGO and ZnS-15%RGO samples. This result suggests a bandgap narrowing of ZnS owing to the coupling in ZnS-RGO nanocomposites [30,39].

Fig. 10 shows the UV–vis absorption spectrum of the MB aqueous solution degraded by ZnS-15%RGO nanocomposites within 240 min.

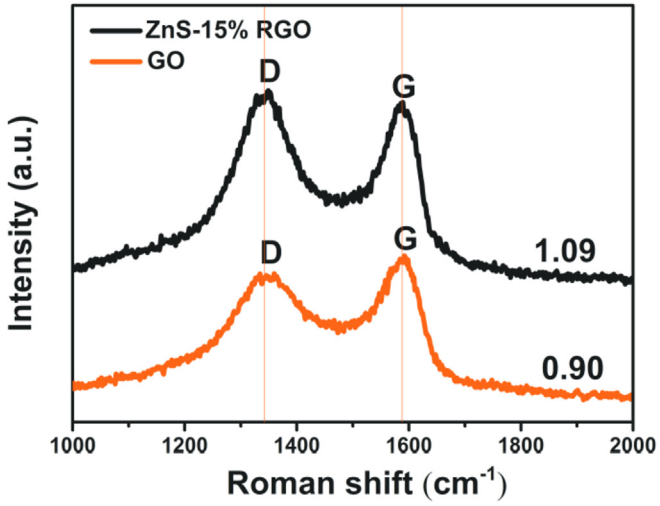


**Fig. 6.** Raman spectra of the pristine GO and ZnS-15%RGO samples.

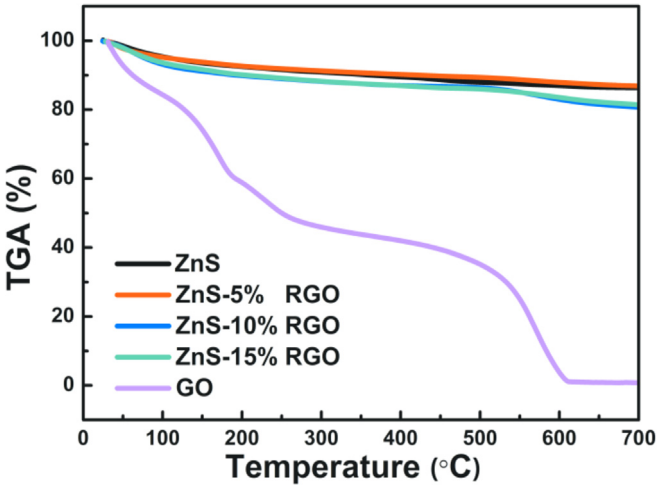


**Fig. 7.** TGA curves of the different samples.

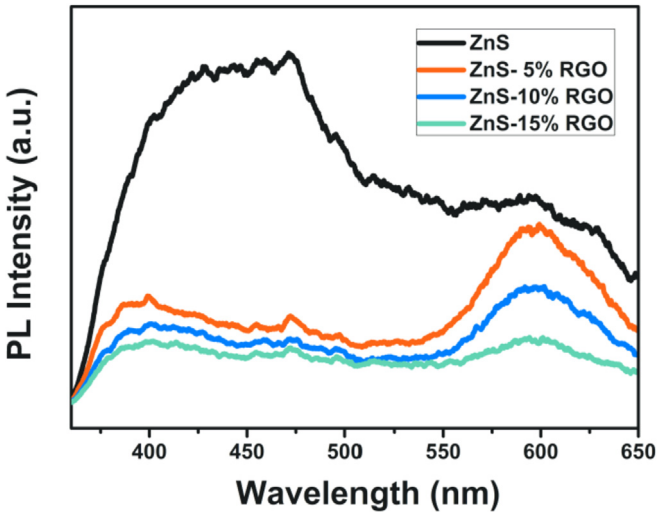


**Fig. 8.** PL spectra of various samples with an excitation wavelength of 330 nm.

The intensity of the maximum absorption peak of MB (663 nm) decreased with the irradiation time increasing, which is owing to the photocatalytic degradation of MB as shown in Fig. 11a. It need to be noted that there are two mutually improved degradation processes

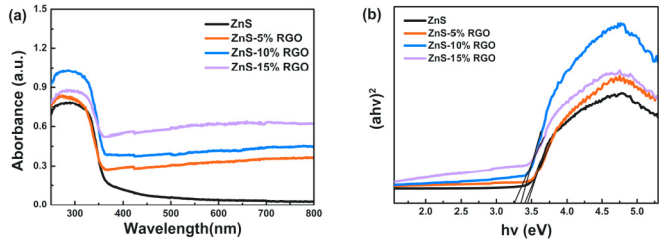


**Fig. 9.** (a) UV–Vis diffuse reflectance spectra and (b) the band gap analysis plot obtained via the transformation based on the Kubelka Munk function of pure ZnS and ZnS-RGO with different weight ratios of RGO.

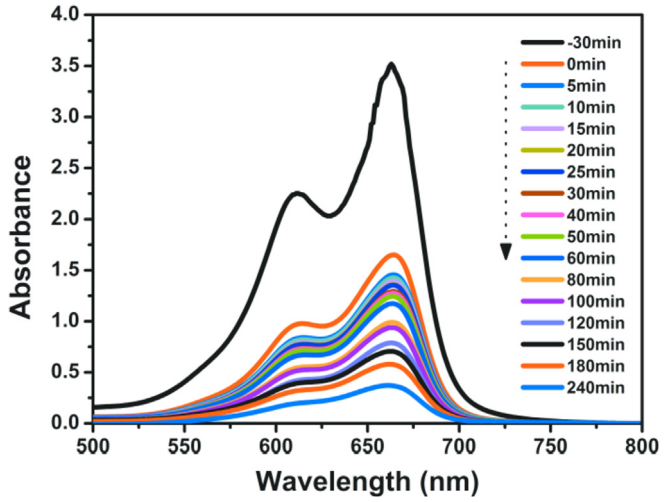


**Fig. 10.** UV–Vis absorption spectra of MB solution in the presence of ZnS-15% RGO.

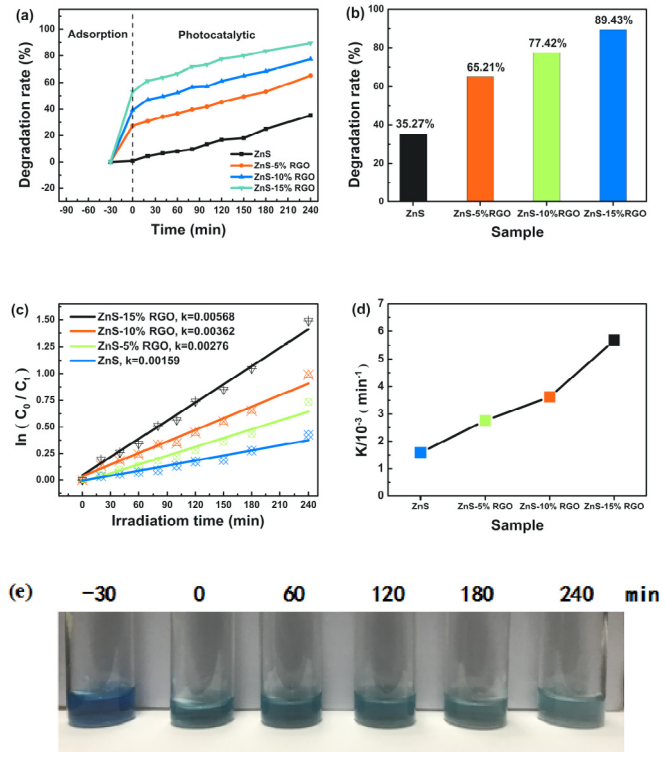


**Fig. 11.** MB degradation (a) curves and (b) bar graphs of the different samples, (c) pseudo-first order kinetics study of MB photodegradation using all samples, (d) the rate constant k of the different samples, (e) Optical images before and after MB degradation process of ZnS-15%RGO.

(adsorption region: −30-0 min, photocatalytic region: 0–240 min). The adsorption efficiency of graphene for MB dye macromolecules plays an important role in photocatalytic degradation of MB aqueous solution. Degradation rate of MB (20 mg/L) using ZnS-15%RGO nanocomposite can rapidly reach 53% in the dark and finally a maximum of 89.43% after 240 min, while pure ZnS nanoparticles exhibited lower visible-light photocatalytic degradation rate of only 35.27% after 240 min. It can be seen from Fig. 11b that the degradation rate of ZnS-RGO samples was enhanced with the weight ratio of RGO increasing. The addition of an appropriate amount of graphene would significantly enhance the photocatalytic activity. However, some groups report that excessive addition of black RGO would block the light into the depth of MB solution, thus leading to the decreased photoactivity [30,31].

Photocatalytic reaction occurred on the surface of samples, which can be represented by the Langmuir-Hinshelwood model [40]. The photocatalytic degradation rate constant of MB by samples was investigated with the help of pseudo-first order kinetics model, which is expressed by the following equation:

$$\ln(C_0/C_t) = kt \quad (3)$$

where $C_0$ is the initial concentration of MB after dark adsorption, $C_t$ is the final concentration after a period of time $t$, and $k$ is the surface reaction rate constant.

The first-order plot for different samples is shown in Fig. 11c. The calculation results of the surface reaction rate constant for ZnS-RGO nanocomposites (0%, 5%, 10% and 15%) were 0.0015, 0.0030, 0.0041 and 0.0064 $min^{-1}$, respectively [41]. The rate constant of ZnS-15% RGO was four times more than that of pure ZnS (Fig. 11d). Optical images before and after MB degradation process of ZnS-15%RGO is provided in Fig. 11e, the color of MB aqueous solution faded after 240 min. A comparison with some previous literature is made for different dyes removal efficiency as seen in Table 1, our ZnS-RGO nanocomposites reported in this work shows a better visible light degradation of MB aqueous solution and is promising for photo-degradation applications.

Different dye degradation curves of ZnS-15%RGO is shown in Fig. 12a, the degradation rate of MB using ZnS-15%RGO finally reached a maximum of 89.43% after 240 min, while the degradation rate of RhB was only 29.57%, which might be related to the molecular structure of dye. It indicates that visible-light photocatalytic activity of ZnS-RGO possesses a certain degree of selectivity for dyes. In order to understand superoxide and hydroxyl radicals which one is actually performing the photocatalytic degradation, a radical trapping experiment in the presence of 1 mmol of benzoquinone (BQ) as a superoxide radical scavenger ($\bullet O_2^-$) and 10 mmol of tertiary butanol (TBA) as a hydroxyl radical scavenger (•OH) was conducted. As shown in Fig. 12b, the degradation rate of MB in the dark was enhanced slightly with the addition of BQ, while the maximum degradation rate was no obvious change. The degradation of MB was inhibited slightly by TBA. It reveals that both superoxide and hydroxyl radicals play a significant role in the photocatalytic degradation process [18,19].

Notably, the UV–vis spectra of ZnS-RGO samples mentioned above revealed that the wide band gap of ZnS with the addition of RGO reduced to a certain extent, but not reaching to the visible light region yet. Therefore, ZnS-RGO samples should not show visible light photocatalytic activities theoretically. But when we performed the photocatalytic degradation of MB solution experiment under the visible light, ZnS-RGO samples exhibited enhanced photocatalytic activities. According to the literature [21,31], the visible light photocatalytic properties of ZnS-RGO samples are ascribed to the new role of RGO as an organic dye-like photosensitizer. A simple photocatalytic reaction mechanism (Fig. 13) is proposed as follows: First, RGO could be excited from the ground state to excited state (RGO → $RGO^*$) under visible light irradiation. Then, the electrons in the excited state of $RGO^*$ are transferred to the conduction band (CB) of ZnS, causing a charge transfer and separation. Consequently, the photoexcited electrons could transfer to the surface of samples and react with molecular $O_2$ to yield $\bullet O_2^-$. Furthermore, the superoxide radicals could generate the hydroxyl radicals. Finally, the organic dye pollutants would be degraded by these superoxide radicals and hydroxyl radicals into $CO_2$ and $H_2O$ [42]. The whole system undergoes the reactions as follows:

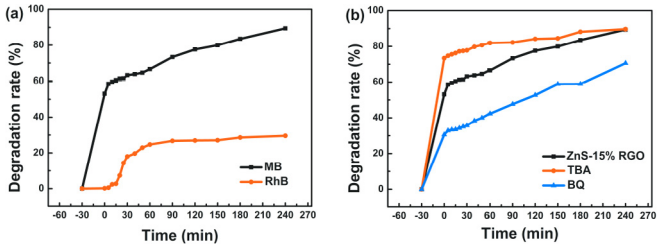


**Fig. 12.** (a) Different dye degradation of ZnS-15%RGO, (b) Effects of different scavengers on the degradation of MB in the presence of ZnS-15%RGO.

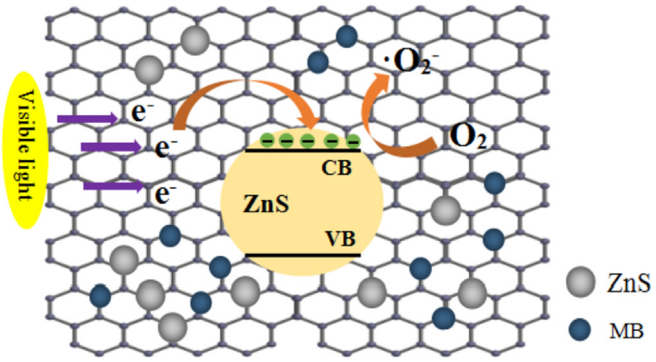


**Fig. 13.** A facile photocatalytic reaction mechanism for the MB degradation by ZnS-RGO.

$$RGO + hv \rightarrow RGO^*(e^-) \quad (4)$$

$$RGO(e^-) + ZnS \rightarrow ZnS(e^-) + RGO \quad (5)$$

$$ZnS(e^-) + O_2 \rightarrow ZnS + \bullet O_2^- \quad (6)$$

$$\bullet O_2^- + 2H^+ + e^- \rightarrow H_2O_2 \quad (7)$$

$$H_2O_2 + e^- \rightarrow \bullet O\,H + OH^- \quad (8)$$

$$\bullet O\,H + MB \rightarrow CO_2 + H_2O \quad (9)$$

Such a MB photocatalytic degradation measurement directly proves RGO can act as an organic dye-like photosensitizer rather than an

**Table 1**
Comparison of degradation rate of various materials towards dyes.

| Material | Light source | Dye | Time (min) | Degradation rate | Ref |
|---|---|---|---|---|---|
| ZnS nanospheres-rGO | UV light | Norfloxacin (20 mg/L) | 240 | 92% | [32] |
| ZnS/rGO (15%) | sunlight | Methyl blue (10 mg/L) | 150 | 86% | [42] |
| ZnS/RGO | UV light | Methyl orange (20 mg/L) | 60 | 75% | [43] |
| ZnS-RGO | UV light | Direct Blue 53 | 100 | 97.4% | [44] |
| ZnS-15%RGO | Visible light | Methyl blue (20 mg/L) | 240 | 89.43% | This work |

electron reservoir. This new photocatalytic mechanism is different from the previous research and would provide a novel thought on designing better photocatalysts of GR-based composites in the future.

## 4. Conclusions

In summary, the ZnS-RGO nanocomposites have been readily synthesized by a simple one-step hydrothermal reaction. The addition of RGO could prevent the agglomeration and promote the crystallization of ZnS nanoparticles, so ZnS nanoparticles were dispersed uniformly on the surface of graphene sheets. Novel high visible-light photoactivity of ZnS-RGO nanocomposites were obtained by controlling the weight ratio of graphene, which is due to the photosensitization of RGO. Degradation rate of MB using ZnS-15%RGO nanocomposite can rapidly reach 53% in the dark, and finally a maximum of 89.43% after 240 min visible light irradition, and its surface reaction rate constant was about four times higher than that of pure ZnS. The results indicate that the coupling of the semiconductor and graphene could enhance the visible-light photocatalytic activity. This study further expands the application of ZnS-GR composites in visible-light photocatalytic degradation of MB aqueous solution. Our findings can help to prepare novel GR-based photocatalysts with better photocatalytic properties.

## Conflicts of interest

On behalf of all authors, the corresponding author states that there is no conflict of interest.

## Acknowledgment

This work was supported by the Joint Foundation of National Natural Science Foundation of China (Grant No. U1764254), China; 321 talent project of Nanjing (Grant No. 631783), China; 111 Project (D17003), China.

## References

[1] X. Li, J. Wen, J. Low, et al., Design and fabrication of semiconductor photocatalyst for photocatalytic reduction of $CO_2$ to solar fuel, Science China Materials 57 (1) (2014) 70–100.
[2] H. Huang, N. Huang, Z. Wang, et al., Room-temperature synthesis of carnation-like ZnO@AgI hierarchical nanostructures assembled by AgI nanoparticles-decorated ZnO nanosheets with enhanced visible light photocatalytic activity, J. Colloid Interface Sci. 502 (2017) 77.
[3] X.X. Chang, J.L. Gong, On the importance of surface reactions on semiconductor photocatalysts for solar water splitting, Acta Physico-Chim. Sin. 32 (1) (2016) 2–12.
[4] X. Rui, H. Tan, Q. Yan, Nanostructured metal sulfides for energy storage, Nanoscale 6 (17) (2014) 9889.
[5] C.H. Lai, M.Y. Lu, L.J. Chen, Metal sulfide nanostructures: synthesis, properties and applications in energy conversion and storage, J. Mater. Chem. 22 (1) (2011) 1580–1581.
[6] X. Fang, T. Zhai, U.K. Gautam, et al., ZnS nanostructures: from synthesis to applications[J], Prog. Mater. Sci. 56 (2) (2011) 175–287.
[7] R. Ma, C. Levard, J.D. Judy, et al., Fate of zinc oxide and silver nanoparticles in a pilot wastewater treatment plant and in processed biosolids, Environ. Sci. Technol. 48 (1) (2015) 104–112.
[8] S. Singla, B. Pal, Highly porous ZnS microspheres for superior photoactivity after Au and Pt deposition and thermal treatment, Mater. Res. Bull. 48 (11) (2013) 4867–4871.
[9] X. Xu, L. Hu, N. Gao, et al., Controlled growth from ZnS nanoparticles to ZnS–CdS nanoparticle hybrids with enhanced photoactivity, Adv. Funct. Mater. 25 (3) (2015) 445–454.
[10] L. Yin, D. Zhang, D. Wang, et al., Size dependent photocatalytic activity of ZnS nanostructures prepared by a facile precipitation method, Mater. Sci. Eng. B 208 (2016) 15–21.
[11] A. Asfaram, M. Ghaedi, S. Hajati, et al., Simultaneous ultrasound-assisted ternary adsorption of dyes onto copper-doped zinc sulfide nanoparticles loaded on activated carbon: optimization by response surface methodology, Spectrochim. Acta Part A Molecular & Biomolecular Spectroscopy 145 (2015) 203–212.
[12] J. Ran, G. Gao, F.T. Li, et al., $Ti_3C_2$ MXene co-catalyst on metal sulfide photo-absorbers for enhanced visible-light photocatalytic hydrogen production, Nat. Commun. 8 (2017) 13907.
[13] M. Jamshidi, M. Ghaedi, K. Dashtian, et al., Highly efficient simultaneous ultrasonic assisted adsorption of brilliant green and eosin B onto ZnS nanoparticles loaded activated carbon: artificial neural network modeling and central composite design optimization, Spectrochim. Acta Part A Molecular & Biomolecular Spectroscopy 153 (3) (2016) 257–267.
[14] F. Bonaccorso, L. Colombo, G. Yu, et al., 2D materials. Graphene, related two-dimensional crystals, and hybrid systems for energy conversion and storage, Science 347 (6217) (2015) 1246501.
[15] A.C. Ferrari, F. Bonaccorso, V. Fal'Ko, et al., Science and technology roadmap for graphene, related two-dimensional crystals, and hybrid systems, Nanoscale 7 (11) (2015) 4598–4810.
[16] R. Raccichini, A. Varzi, S. Passerini, et al., The role of graphene for electrochemical energy storage, Nat. Mater. 14 (3) (2015) 271–279.
[17] F. Bonaccorso, L. Colombo, G. Yu, et al., 2D materials. Graphene, related two-dimensional crystals, and hybrid systems for energy conversion and storage, Science 347 (6217) (2015) 1246501.
[18] X. Lu, F. Deng, M. Liu, et al., The regulation on visible-light photocatalytic activity of $CuInS_2$, by different Cu/In molar ratio, Mater. Chem. Phys. 212 (2018) 372–377.
[19] H. Xiufen, D. Fang, H. Weiya, et al., The band structure control of visible-light-driven rGO/ZnS-$MoS_2$, for excellent photocatalytic degradation performance and long-term stability[J], Chem. Eng. J. 350 (2018) 248–256.
[20] Q. Li, X. Li, S. Wageh, et al., CdS/Graphene nanocomposite photocatalysts, Advanced Energy Materials 5 (14) (2015).
[21] Y. Zhang, Z.R. Tang, X. Fu, et al., Engineering the unique 2D mat of graphene to achieve graphene-$TiO_2$ nanocomposite for photocatalytic selective transformation: what advantage does graphene have over its forebear carbon nanotube? ACS Nano 5 (9) (2011) 7426–7435.
[22] H. Fan, X. Zhao, J. Yang, et al., ZnO–graphene composite for photocatalytic degradation of methylene blue dye, Catal. Commun. 29 (48) (2012) 29–34.
[23] Z. Chen, N. Zhang, Y.J. Xu, Synthesis of graphene–ZnO nanorod nanocomposites with improved photoactivity and anti-photocorrosion, CrystEngComm 15 (15) (2013) 3022–3030.
[24] J. Yi, J.M. Lee, W.I. Park, Vertically aligned ZnO nanorods and graphene hybrid architectures for high-sensitive flexible gas sensors, Sensor. Actuator. B Chem. 155 (1) (2011) 264–269.
[25] J. Cao, Q. Liu, D. Han, et al., Highly enhanced photocatalytic properties of ZnS nanowires–graphene nanocomposites[J], RSC Adv. 4 (58) (2014) 30798–30806.
[26] B. Zeng, X. Chen, Q. Tang, et al., Ordered mesoporous necklace-like ZnS on graphene for use as a high performance photocatalyst, Appl. Surf. Sci. 308 (8) (2014) 321–327.
[27] Y.J. Yang, One-pot synthesis of reduced graphene oxide/zinc sulfide nanocomposite at room temperature for simultaneous determination of ascorbic acid, dopamine and uric acid, Sensor. Actuator. B Chem. 221 (2015) 750–759.
[28] Y. Zhang, Z.R. Tang, X. Fu, et al., $TiO_2$-graphene nanocomposites for gas-phase photocatalytic degradation of volatile aromatic pollutant: is $TiO_2$-graphene truly different from other $TiO_2$-carbon composite materials? ACS Nano 4 (12) (2010) 7303–7314.
[29] Baojun Li, Huaqiang Cao, ZnO@graphene composite with enhanced performance for the removal of dye from water, J. Mater. Chem. 21 (10) (2011) 3346–3349.
[30] F. Wang, M. Zheng, C. Zhu, et al., Visible light photocatalytic $H_2$-production, activity of wide band gap ZnS nanoparticles, based on the photosensitization of graphene, Nanotechnology 26 (34) (2015) 345402.
[31] Y. Zhang, N. Zhang, Z.R. Tang, et al., Graphene transforms wide band gap ZnS to a visible light photocatalyst. The new role of graphene as a macromolecular photosensitizer, ACS Nano 6 (11) (2012) 9777–9789.
[32] J. Bai, Y. Li, P. Jin, et al., Facile preparation 3D ZnS nanospheres-reduced graphene oxide composites for enhanced photodegradation of norfloxacin, J. Alloy. Comp. 729 (2017) 809–815.
[33] S. Zhang, J. Yang, B. Chen, et al., One-step hydrothermal synthesis of reduced graphene oxide/zinc sulfide hybrids for enhanced tribological properties of epoxy coatings, Surf. Coating. Technol. (2017) 326.
[34] S. Pan, X. Liu, ZnS–Graphene nanocomposite: synthesis, characterization and optical properties, J. Solid State Chem. 191 (7) (2012) 51–56.
[35] J. Cao, Q. Liu, D. Han, et al., One-step hydrothermal synthesis of shape-controlled ZnS–graphene oxide nanocomposites, J. Mater. Sci. Mater. Electron. 26 (2) (2015) 646–650.
[36] W. Qin, D. Li, X. Zhang, et al., ZnS nanoparticles embedded in reduced graphene oxide as high performance anode material of sodium-ion batteries, Electrochim. Acta 191 (2016) 435–443.
[37] M. Sookhakian, Y.M. Amin, R. Zakaria, et al., Significantly improved photocurrent response of ZnS-reduced graphene oxide composites, J. Alloy. Comp. 632 (2015) 201–207.
[38] H. Li, F. Xie, W. Li, et al., Preparation and adsorption capacity of porous $MoS_2$ nanosheets, RSC Adv. 6 (107) (2016).
[39] M.Q. Yang, Y.J. Xu, Basic principles for observing the photosensitizer role of graphene in the graphene–semiconductor composite photocatalyst from a case study on graphene–zno, J. Phys. Chem. C 117 (42) (2016) 21724–21734.
[40] Y. Qin, Z. Sun, W. Zhao, et al., Effect of $S^{2-}$, donors on synthesizing and photocatalytic degrading properties of ZnS/RGO nanocomposite, Appl. Phys. A 123 (5) (2017) 355.
[41] B. Sheng, J. Liu, Z. Li, et al., Effects of excess sulfur source on the formation and photocatalytic properties of flower-like $MoS_2$, spheres by hydrothermal synthesis, Mater. Lett. 144 (9) (2015) 153–156.
[42] H.R. Azimi, M. Ghoranneviss, S.M. Elahi, et al., Excellent photocatalytic performance under visible-light irradiation of ZnS/rGO nanocomposites synthesized by a green method, Front. Mater. Sci. 10 (4) (2016) 1–9.
[43] Y. Qin, Z. Sun, W. Zhao, et al., Improved photocatalytic properties of ZnS/RGO nanocomposites prepared with GO solution in degrading methyl orange, Nano-Structures & Nano-Objects 10 (2017) 176–181.
[44] S. Dutta, S. Chatterjee, I. Mukherjee, et al., Fabrication of ZnS hollow spheres and RGO-ZnS nanocomposite using Cysteamine as novel sulphur source: photocatalytic performance on industrial dyes and effluent, Ind. Eng. Chem. Res. 56 (16) (2017).